The Astrophysical Journal, 846:92 (14pp), 2017 September 10 https://doi.org/10.3847/1538-4357/aa85e1
© 2017. The American Astronomical Society. All rights reserved.
OPEN ACCESS

A Model of the Solar Chromosphere: Structure and Internal Circulation

P. Song
Space Science Laboratory and Department of Physics, University of Massachusetts Lowell, USA
Received 2017 April 11; revised 2017 August 9; accepted 2017 August 9; published 2017 September 5

Abstract

A model of the solar chromosphere that consists of two fundamentally different regions, a lower region and an upper region, is proposed. The lower region is covered mostly by weak locally closed magnetic field and small network areas of extremely strong, locally open field. The field in the upper region is relatively uniform and locally open, connecting to the corona. The chromosphere is heated by strong collisional damping of Alfvén waves, which are driven by turbulent motions below the photosphere. The heating rate depends on the field strength, wave power from the photosphere, and altitude in the chromosphere. The waves in the internetwork area are mostly damped in the lower region, supporting radiation in the lower chromosphere. The waves in the network area, carrying more Poynting flux, are only weakly damped in the lower region. They propagate into the upper region. As the thermal pressure decreases with height, the network field expands to form the magnetic canopy where the damping of the waves from the network area supports radiation in the whole upper region. Because of the vertical stratification and horizontally nonuniform distribution of the magnetic field and heating, one circulation cell is formed in each of the upper and lower regions. The two circulation cells distort the magnetic field and reinforce the funnel-canopy-shaped magnetic geometry. The model is based on classical processes and is semi-quantitative. The estimates are constrained according to observational knowledge. No anomalous process is invoked or needed. Overall, the heating mechanism is able to damp 50% of the total wave energy.

Key words: convection – magnetohydrodynamics (MHD) – radiative transfer – stars: chromospheres – Sun: chromosphere – Sun: transition region

1. Introduction

The physical processes in the solar chromosphere are poorly understood, although they play important roles in setting up the conditions for the formation of the corona and eventually the solar wind. A large fraction of the mechanical energy, $\sim 10^7$ erg cm^{-2} s^{-1} (e.g., Withbroe & Noyes 1977; Ulmschneider 2001), which is in the form of waves or perturbations, is dissipated within the observed thickness of the chromosphere, $\sim$2000 km (e.g., Avrett & Loeser 2008). The conventional wisdom is that most of the wave energy is carried by oscillations with period near 300 s. Given that the sonic and Alfvén speeds in the chromosphere are about 10 km s^{-1}, the wavelength of $\sim$3000 km is of the same order as the thickness of the chromosphere, namely, the damping of the waves has to be extremely heavy. In the network areas, the magnetic field is extremely strong, and the wavelength can be much greater than the thickness of the chromosphere. If the wave energy flux responsible for most of the chromospheric heating and consequent radiation is concentrated in these areas, significantly damping the waves within the chromosphere is anything but impossible. This simple assessment explains why coronal heating has been an outstanding problem for so long following conventional approaches. Here we should point out that the key issue is not about the total energy converted or radiated, as is often discussed in conventional thinking, but the rate of the conversion. The required average heating rate of the total dissipation with the observed thickness of the chromosphere is 5×10^{-2} erg cm^{-3} s^{-1}. If the heating rate of a model is lower than required, the total heating can be proportionally large if one assumes a greater wave source power (e.g., Ulmschneider et al. 2005), an approach that would eventually be inconsistent with either the observed available wave power or with the total leftover energy in the corona and solar wind if the thickness of the chromosphere is limited by the observed wave power. Similarly, if the heating rate of a model is not sufficiently large, the required total amount of energy conversion can always be achieved over a longer spatial distance (e.g., Cranmer et al. 2007), i.e., a thicker chromosphere, much greater than the observed one. Alternatively, when the heating rate is not sufficient, models often invoke anomalous processes or artificially enhance the dissipation coefficients (e.g., Martínez-Sykora et al. 2012) in order to derive a desirable, rather than physical, dissipation or heating rate—an approach that remains prevailing in the field and is often considered the solution to the problem.

Upon reviewing our knowledge about the heating of the solar atmosphere, Song & Vasyliūnas (2011) found that the inability to identify the dominant mechanisms for heating the atmosphere for so many decades since its recognition in 1943 (Edlén 1943) might have been due to the confusion of two physical constraints used in investigations, i.e., the confusion of radiative cooling with the temperature rising at the transition region and in the corona, and the possible confusion of the "remotely observed" dominant chromospheric perturbations with the source of energy for wave heating. First, radiative cooling and temperature rise do not need to take place in the same region. Because the emission can easily be produced in the presence of a large amount of neutral atoms, radiative cooling takes place mostly in the chromosphere, where the fluid is weakly ionized and the density is high. On the other hand, emission is much weaker from the corona, where the fluid is nearly fully ionized and the density is low. The heating rate needed to raise the temperature of the tenuous gas there is very small because there is nearly no radiative loss

Original content from this work may be used under the terms of the Creative Commons Attribution 3.0 licence. Any further distribution of this work must maintain attribution to the author(s) and the title of the work, journal citation and DOI.

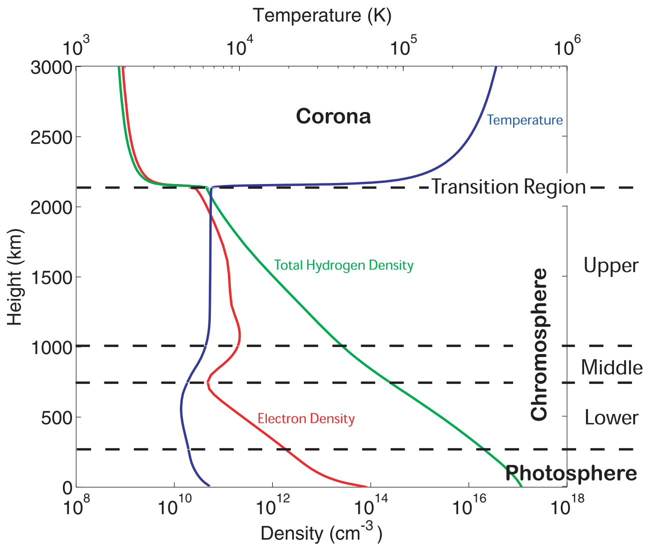

Figure 1. Temperature (blue line), total hydrogen number density (green line), and electron number density (red line; Avrett & Loeser 2008). Dashed lines mark the regionsin the discussion.

when the gas is fully ionized. Compared with the rapid temperature rise at the transition region and in the corona, as shown in Figure 1, the temperature does not change substantially in the chromosphere. When the large radiative loss and the temperature rise occur in different regions, the seemingly contradictory requirements may not be a problem. Although generally referred to as "coronal heating," the required heating in the corona is actually only a few percent of the total required heating under quiet-Sun conditions (Withbroe & Noyes 1977).

Second, oscillations with periods around 5 minutes have been convincingly documented mostly with strong magnetic field (e.g., Ulrich 1996; Jess et al. 2009), and the interpretation has been that (a)chromospheric heating is primarily produced by the 5-minute oscillations, and (b) more heating is provided in strong magnetic field regions. The irony in this line of argument is that because, as discussed above, the available wave power is of the same order as the required heating rate, much of the wave energy should have been consumed to become heat and radiated away. It should not have been observed as wave oscillation power in regions significantly far from the source. The observed oscillations may just be the residues in small areas after the damping/heating processes. If the waves in these areas are not strongly damped, contrary to both interpretations (a) and (b) above, they may not actually contribute significantly to the heating that supports the large-scale properties of the chromosphere. Although Alfvén waves were found to be heavily damped in high frequencies (e.g., Osterbrock 1961; De Pontieu et al. 2001; Leake et al. 2005) and Alfvén waves with 5-minute oscillations were found weakly damped, the focus of Alfvén wave damping has remained on periods around 5 minutes.

Alternatively, when the magnetic field is weak, the perturbations can be treated as acoustic waves (e.g., Narain & Ulmschneider 1990, 1996). Because of the rapid decrease in density, vertically propagating acoustic waves may evolve into nonlinear or shock waves, which lead to dissipative heating (e.g., Ulmscheider 1981; Mihalas & Toomre 1982; Ulmschneider et al. 2005). The heating rate in this process is mainly determined by the vertical component of the velocity perturbations. There is an issue of how much acoustic wave flux is available upward from the photosphere. Some observations have indicated that the available acoustic wave power is not sufficient to support the required heating (e.g., Fossum & Carlsson 2005; Kalkofen 2007), but others have shown higher fluxes in localized areas (Bello Gonzalez et al. 2010). If the energy flux is adequate, perturbations of higher frequencies may steepen more quickly and heat the lower region. The lower frequencies may propagate to higher regions before steepening.

These conventional heating mechanisms from previous investigations, either from strong field areas in Alfvén wave heating based on 5-minute oscillations or without magnetic effects in acoustic or shock heating, either provide only a few percent of the required heating rate or occur only in higher altitudes. In some sense, the negative conclusion of previous studies is consistent with some of the assumptions that were incorrectly made in those theoretical investigations, such as the wave energy flux being nearly constant with height. After all, if the energy flux is constant with height, the waves are not damped and can be observed above the source, and therefore they should not produce much heat. In contrast to the weak heating rates derived from these models based on "classical" theories, to enhance the heating rate, many numerical simulation models artificially increase the dissipation via extremely large magnetic diffusion and/or viscosity. Although these artificially large dissipations do provide sufficiently large heating rates, they also produce turbulence in the simulation results. Therefore, turbulent heating becomes a commonly accepted heating mechanism. We should, however, note the logical hole in this line of argument.

In a self-consistent *local* treatment, Song & Vasyliūnas (2011) found that collisional MHD wave damping consists of two effects, i.e., Ohmic and frictional heating in partially ionized plasma (Vasyliūnas & Song 2005), which has become a new field of research in recent years (e.g., Khodachenko et al. 2004; Khomenko & Collados 2012; Shelyag et al. 2013; Soler et al. 2013; Zaquarashvili et al. 2013). Ohmic heating is most effective when the field is weak, and frictional heating when the field is strong. Song & Vasyliūnas evaluated the heating rate due to the damping of Alfvén waves, which originated from the *horizontal* oscillations in the photosphere. Recognizing that the photosphere is a region of highly turbulent fluid, the source of the waves is unlikely to have a narrow frequency band near 1/5 minutes, but the waves may have been cascaded from this frequency to higher frequencies. Assuming a power-law spectrum from the photosphere, the heating rate from this collisional heating mechanism is sufficiently large to satisfy the observational constraints. The power in higher frequencies is damped more heavily so that the remaining (undamped) power is around 5 minutes, as observed (e.g., Fossum & Carlsson 2005; Reardon et al. 2008). The heating rate derived from the model is higher in the lower chromosphere and in weaker magnetic field areas so that more power remains in stronger magnetic field areas and propagates to the upper region. Although Song & Vasyliūnas (2011) demonstrated that the collisional damping of the Alfvén waves, depending on the field strength, can be as strong as 90% through the chromosphere and that the heating is generally heavier in the lower altitudes than in the higher altitudes, quantitatively, the heating rate as a function of height is significantly different from those shown by Withbroe & Noyes (1977) and Vernazza et al. (1981). Therefore, Song & Vasyliūnas (2011) cannot be considered as having been validated by Withbroe & Noyes (1977) and Vernazza et al. (1981). Nevertheless, Tu & Song (2013) confirmed the analytical results of Song & Vasyliūnas (2011) with numerical simulations that are based on the same set of governing equations and removed a few approximations employed in the analytical model, such as wave propagation without reflection and a simple superposition of multiple frequency waves. Although the mechanism is efficient, its application to the chromosphere, in particular the properties of the wave source, i.e., its height and spectral strength, remain to be tested. Note that in this model, the theory and simulations are based on classical processes and no anomalous process is invoked. The function of the turbulence invoked in the model is only to provide the wave spectrum at the photospheric boundary and is not actually involved directly in the heating process.

Song & Vasyliūnas (2014) investigated the effects of nonuniform magnetic field distribution in the photosphere. They found that the strong heating in the weak field area of the lower chromosphere is due to Ohmic heating. In the upper chromosphere, where the density is much lower, the dominant heating is via friction between ion and neutral flows above the strong field in the lower region. In the weak field area of the upper region, the heating rate is low due to the diminished available wave power as a result of heavy damping.

In Section 2, we put forward a coherent scenario of the chromosphere under quiet conditions with the spatial scale of a supergranule, following the initial proposal of Song & Vasyliūnas (2014) but providing more details and justifications as well as the connection among the different elements of the scenario. We first introduce, in Section 2.1, the methodology to be employed in this study: theoretical modeling. After introducing the governing equations in Section 2.2, two limiting situations are discussed: in Section 2.3, we present the overall average structure of the chromosphere with heating and radiation processes and the field geometry expected from the model, and in Section 2.4, we discuss the quasi-steady-state chromosphere with the formation of circulation cells. Finally, in Section 3, we summarize the main findings with discussions.

2. Model of the Chromosphere under Quiet Conditions

Since our model deals with inhomogeneity in both vertical and horizontal directions, to avoid confusion in the following discussion, we use "regions" for vertical differences and "areas" for horizontal differences. We assume that near the photospheric boundary under quiet conditions, the source is at $z = 220$ km. This is a substantial update from earlier evaluations of the heating rate (Song & Vasyliūnas 2011, 2014; Tu & Song 2013), which assumed the source to be at $z = 0$ km. At $z = 0$ km, the optical depth τ_{500} is 1; at $z = 220$ km, the optical depth drops to about 0.1, the conventional separation of the photosphere and chromosphere (e.g., Cranmer et al. 2007). The region below 220 km is beyond the scope of this investigation, because the optical depth is large and radiative absorption and scattering dominate. Our model describes the processes above this lower boundary up to the height where the temperature starts a rapid rise before reaching the transition region. We represent, near the photospheric boundary, a quiet-time chromospheric supergranule as a two-dimensional slab with a small strong field area in the middle. If the network field strength is 1 kG at $z = 0$ with a width of 500 km (Judge 2006), at the lower boundary $z = 220$ km, we choose $B_s \sim 750$ G, the magnetic pressure of which would balance the thermal pressure given by the semi-empirical model (Avrett & Loeser 2008). A significantly stronger magnetic pressure would lead to a further expansion of the network, which reduces the field strength so that a force balance can be reached. At 220 km with $B_s \sim 750$ G, with magnetic flux conservation, the half-width of the network would be 333 km. We then assume that the network half-width $D \sim 300$ km. The internetwork occupies the rest 2D space of the supergranule in a horizontal scale of half-width $L \sim 15{,}000$ km. In the internetwork, the average magnetic field is a few Gauss and relatively random. This field distribution in the lower chromosphere is in general consistent with that of Judge (2006) and Wöger et al. (2009). The thickness of the chromosphere is about 2000 km. In the following discussion, we refer to the lower chromosphere as the region from $z = 220$ to $z = 700$ km, and the upper chromosphere from $z = 1000$ km to the transition region, which is at $z = 2140$ km according to the semi-empirical model. The mid-altitudes from $z = 700$ km to $z = 1000$ km are physically the upper region in development, or the field expansion region. The choice of 1000 km is somewhat arbitrary but is based on a hint from the change in the temperature profile at this height in Figure 1.

2.1. Methodology

The method employed in this study is the so-called "theoretical modeling" (e.g., Song & Vasyliūnas 2010), a method that has been widely used in space physics. But with the increased computational capability over the last few decades, a common perception is that theoretical modeling is not needed because if a theoretical model is correct, simulations have to be able to show it. This is true, but its reverse is not necessarily true, i.e., a simulation may or may not describe a system relevant to the problem of the study as discussed in the introduction.

Theoretical modeling links observations of different types from different places with physical laws. The objective of this study is to understand the controlling processes that are most likely to produce the observed properties based on physical laws. It provides a guide to observational interpretations and ensures that the numerical simulation studies are relevant to the systems they set out to simulate. For example, as mentioned in the introduction, it is a common practice for numerical MHD simulation models to invoke dissipation that is a few orders of magnitude more than justifiable values from experimental one. Although these simulations may have justified these unsupported values with some vague arguments, such as anomalous processes, they may actually be irrelevant to the system they are simulating, even if there are some similarities between the observations and simulation results, because their governing equations are overwhelmed by the artificially inflated dissipation terms. It is interesting to note that very often, these similarities may be in terms of similar complexity between a simulated image and observed one.

This method is guarded by and requires a careful-order analysis, i.e., the identified processes have to be consistent with the leading terms in the governing equations with the ballpark observations of interest. When modeling the chromosphere, there are a few controlling observations: the overall temperature profile of the chromosphere, the available wave energy flux in the wave frequency range of interest to drive the system, the total radiation from the whole region, and the highly inhomogeneous magnetic field distribution and the range of its strength at the photospheric boundary. These are the key pieces of the puzzle of the chromosphere. There are still many more less important pieces. A successful theoretical model has to connect most of these main pieces with physical laws, and the connections, such as mass conservation, energy conservation, momentum conservation, and Maxwell's equations, have to be correct up to the order of magnitude of the model. Of course, different models may choose to follow the "classical laws" or a different set of laws, such as turbulence. In this case, we, however, require these models to be specific up to the order of magnitude, in particular for the dissipation mechanisms and their magnitudes.

In this study, we use the semi-empirical model as the ballpark values of the chromospheric system and follow classical laws, which are standardized to partially ionized, collisional, radiative, multifluid magnetohydrodynamics, (e.g., Song & Vasyliūnas 2011, 2014). Simplifying approximations are made based on the leading terms of the processes under analysis.

2.2. Governing Equations

Although the governing equations include the complete set of three-fluid collisional MHD equations, our focus is on the force balance and energy conservation. We will not repeat the wave analysis part of the MHD theory and the electron fluid aspect. Interested readers may find the detailed derivation and discussion in Song et al. (2005), Song & Vasyliūnas (2011, 2014), and references therein. We defer the discussion of the aspects associated with the differences between the ion fluid and neutral fluid to Section 2.4 and start our treatment of the neutrals and plasma in the chromosphere together as a partially ionized single fluid with an ionization fraction of $\alpha = N_e/N$, where $N = N_i + N_n$ is the total number density of the atoms. The momentum equation is

$$\rho(d/dt)\boldsymbol{V} = -\nabla P + \boldsymbol{J} \times \boldsymbol{B} + \rho\boldsymbol{g}, \tag{1}$$

where $d/dt = \partial/\partial t + \boldsymbol{V}\boldsymbol{\cdot}\boldsymbol{\nabla}$ with $\boldsymbol{V}\boldsymbol{\cdot}\boldsymbol{\nabla}$ being the convective derivative; $\boldsymbol{V}$, $\boldsymbol{J}$, $\boldsymbol{B}$, and $\boldsymbol{g}$ are the bulk velocity of the whole fluid, current, magnetic field, and gravitational acceleration near the surface of the Sun, respectively; $\rho = \rho_e + \rho_i + \rho_n \approx \rho_i + \rho_n = mN$ is the total mass density; $P = P_e + P_i + P_n = (N + N_e)kT = (1 + \alpha)NkT$ is the thermal pressure of the medium, with k being the Boltzmann constant, assuming that the ions are singly ionized, or $N_i = N_e$; and $m_i = m_n = m$, the neutral number density is $N_n = (1 - \alpha)N$. The whole gas, since collisions are frequent, shares the same temperature, or $T_e = T_i = T_n = T$. The subscripts "e," "i," and "n" denote electron, ion, and neutral, respectively.

The dissipation equation (e.g., Song & Vasyliūnas 2014) is

$$\frac{d}{dt}\log\left(\frac{P}{\rho^{5/3}}\right) = \frac{2}{3}\,\frac{Q - R}{P}, \tag{2}$$

where Q is the heating rate and R is the frequency-integrated emission rate. Note that Equation (2) couples the MHD equations with the radiation theory. We do not assume an equation of state, and this is different substantially from many previous theoretical approaches.

In Sections 2.3, we first discuss the locally quasi-static situation, i.e., when the terms on the lhs of Equations (1) and (2) are neglected, in one dimension with two-dimensional generalization. This situation may be considered to be the one described by statistical averages or empirical models. In Section 2.4, we allow a small imbalance between the rhs terms in Equations (1) and (2). Under this condition, the medium starts convecting. In general, the neutral and plasma motions are different, and we discuss the situation for quasi-steady state, i.e., slow evolution, when the partial time derivatives in Equations (1) and (2) can be neglected.

2.3. Local Radiative Equilibrium and Force Balance Condition

2.3.1. Radiative Cooling

Since the optical depth is small in the chromosphere according to our definition, the radiation cannot be treated as either blackbody or graybody emission. The radiative cooling rate R in Equation (2) for an optically thin medium can be derived by integrating the power of the line emissions and is conventionally expressed as (e.g., Cox & Tucker 1969; Anderson & Athay 1989; Schmutzler & Tscharnuter 1991; Cranmer et al. 2007; Schure et al. 2009; Carlsson & Leenaarts 2012)

$$R = N_e N\Lambda = \alpha N^2\Lambda, \tag{3}$$

where Λ depends only on temperature and is the so-called composite radiation function.

To evaluate the density, we adopt the most recent version of the semi-empirical chromospheric model, by Avrett & Loeser (2008), as shown in Figure 1. The ionization fraction, α, can be evaluated either from the radiation model, such as in Cranmer et al. (2007), or from the semi-empirical model of Avrett & Loeser (2008). In the former case, the ionization fraction is a pure function of temperature. As seen in Figure 1, the ionization fraction may not be dependent on the temperature alone. We use the one derived from the semi-empirical model and treat it as an independent variable in the following discussion. We adopt the radiation function $\Lambda(T)$ from Cranmer et al. (2007), which is based on the CHIANTI atomic database (Young et al. 2003). In the temperature range of interest in the chromosphere, 4500 K to ~8000 K, a best fit gives

$$\log_{10}\Lambda = 19.54\log_{10}T - 100.8. \tag{4}$$

Combined with the temperature from Avrett & Loeser (2008), the radiative cooling rate R is shown as the blue curve in Figure 2. We further downward integrate the radiative cooling from the transition region, $W = -\int_z^{2024} R\,dz$, shown as the red line in Figure 2. This curve shows the radiative energy needed to sustain the radiative cooling above a given height. The total radiation in the upper region (>1000 km) is about 4×10^5 erg cm^{-2} s^{-1}. If half of the radiation is observed on the Earth, i.e., is lost from the system, and half of it radiates back toward the solar surface, the amount of the radiative loss, $\sim W/2$, is $\sim 2 \times 10^5$ erg cm^{-2} s^{-1} from the upper chromosphere. If all radiation is produced by the dissipation of the mechanical energy and the total available mechanical energy is $S_0 = 10^7$ erg cm^{-2} s^{-1}, which has been used in most of the conventional models (e.g., Goodman 2000; De Pontieu et al. 2001), the mechanical energy can support at most only the

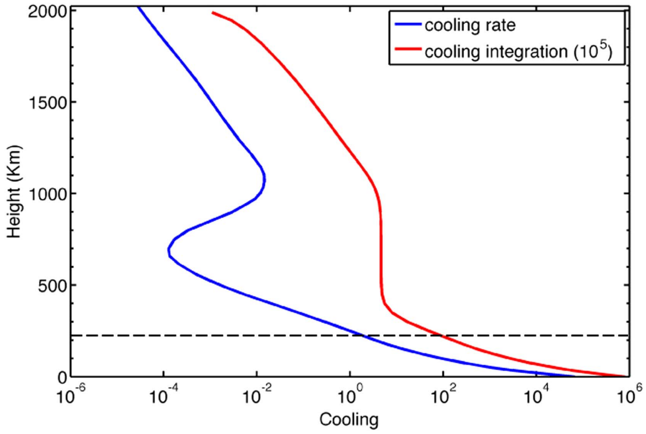

Figure 2. Radiation cooling rate $R = N_e N \Lambda$ (blue line) in erg cm^{-3} s^{-1}, and downward integrated radiation over height starting from 2024 km, W (red line), in 10^5 erg cm^{-2} s^{-1}.

radiation above 220 km, as indicated by the dashed line. Below 220 km, because the optical depth is significantly large, the radiative cooling given by Equation (3) may not be applicable. Therefore, the lower boundary of our model being set at 220 km is consistent with this total energy budget constraint and consistent with the observational definition of the photosphere being below about 250 km (e.g., Aschwanden 2005). An objective of the remaining part of the paper is to demonstrate that the model we derived from this theoretical modeling exercise is able to provide enough heating to support the radiation of $W_0 = 10^7$ erg cm^{-2} s^{-1}, with a reasonable amount of the Poynting flux from the photosphere, at 220 km.

2.3.2. Chromospheric Heating

The heating rate Q in Equation (2) includes contributions from several possible heating mechanisms, such as shock heating Q_{shock}, wave heating Q_{wave}, turbulence heating Q_{turb}, reconnection heating Q_{recon}, and conductive heating Q_{cond}, or

$$Q = Q_{\mathrm{shock}} + Q_{\mathrm{wave}} + Q_{\mathrm{turb}} + Q_{\mathrm{recon}} + Q_{\mathrm{cond}} + \ldots.. \quad (5)$$

The conductive heating $Q_{\mathrm{cond}} = \nabla \bullet \boldsymbol{q}$, where $\boldsymbol{q} = -\kappa \nabla T$ is the heat flux with κ the heat conductivity coefficient (there is a missing minus sign for the heat flux term in Song & Vasyliūnas 2014), is associated with the temperature gradient. Since the temperature does not change much throughout the chromosphere but increases in the last 200 km from 6670 to 8000 K around 2140 km before reaching the transition region, the upper limit of $Q_{\mathrm{cond}} = \kappa_0 \partial^2 (T^{7/2}) / \partial z^2$ can be estimated, given $\kappa_0 = 9.2 \times 10^{-7}/3.5$ erg s^{-1} cm^{-1} K^{-1} (Spitzer 1956), by the heat flux dissipation rate $\partial q / \partial z \sim 10^{-7}$ erg cm^{-3} s^{-1}. It is small when $z < 2000$ km inside the chromosphere, compared with the required heating rate in Figure 2, although it increases rapidly with height in the transition region while radiative cooling, Equation (3), decreases rapidly where the density drops drastically as shown in Figure 1.

Although turbulence, waves, shocks, and reconnection in the timescale of interest are all time-dependent processes, time averages of perturbations have been used to estimate the heating rates. Each of the heating mechanisms invokes specific effects and mathematical treatments. The fact that the chromospheric heating problem remains outstanding for so many decades casts doubt on the significance, applicability, and viability of many of these mechanisms, which have been investigated extensively over decades, to contribute to the chromospheric heating.

There is no question that the free energy responsible for producing chromospheric radiation is provided by photospheric perturbations. These perturbations may be decomposed into a horizontal component and vertical component. The ratio of the horizontal to vertical velocity perturbations can be estimated by the ratio of the two spatial scales for weakly compressible flow. The vertical spatial scale is typically the scale-height, which is about 200 km. Given the sound speed of $\sim$10 km s^{-1}, perturbations of periods longer than 20 s would be dominated by horizontal perturbations. If the granules are of timescales of 10 minutes (longer than 20 s) and horizontal scales of 1000 km (greater than 200 km), the horizontal amplitude of the velocity perturbation is most likely much greater than that of the vertical perturbation except in small areas where the flow is unstable to the buoyancy instability. For the given supergranule geometry, our analysis indicates that the ratio of the horizontal to vertical perturbations is of the order similar to the ratio of the horizontal to vertical spatial scales of the supergranule, which is about $15{,}000/2000 = 7.5$. If we include the effect of two convection cells as will be shown in Section 2.4, the ratio for each cell doubles to 15. Previous analyses (Ulmschneider 2001; Jess et al. 2009) indicated that the ratio can be around $\sim$30. We therefore conclude that it is more likely that the horizontal velocity perturbation is much greater than the vertical one. The energy flux is proportional to the square of the velocity perturbation. Therefore, the Alfvén mode is expected to carry much more energy flux upward from the photosphere than the compressible fast mode.

In principle, horizontal velocity perturbations cannot produce shocks under normal circumstances unless their amplitudes are extremely large, a situation that is rare under quiet conditions. As pointed out by Song & Vasyliūnas (2011), the vertical component of the perturbations can efficiently propagate upward via the fast mode and the horizontal component via the Alfvén mode. In fact, for low beta plasma, the fast mode degenerates with the Alfvén mode and is incompressible in parallel propagation. Therefore, all upward energy in the horizontal perturbations can be carried by the Alfvén mode. The Alfvén mode/wave in our discussion refers to the generic intermediate mode that propagates along or at an angle with the field. If the average field is not vertical or the propagation is not vertical, a correction factor of the cosine propagation angle should be added.

The analysis of Song & Vasyliūnas (2011) is based on 1D geometry. Compared with other mechanisms, the heating mechanism depends only critically on the horizontal perturbation velocity and vertical propagation. In 2D geometry, there are multiple possible modes for propagation. The mechanism described by Song & Vasyliūnas (2011) can be generalized to 2D for either torsional (e.g., Erdelyi & Fedun 2007) or kink mode (De Pontieu et al. 2007) because both of them involve vertically propagating horizontal perturbations. The complication added by the 2D constraints in a cylindrical system is that the perturbation and hence the wave flux may not distribute uniformly horizontally and some modifying factors may be added in detailed models.

There is a singular case in a cylindrical system when the oscillations are horizontally coherent in the radial direction over the whole cylinder and produce a pinch or sausage mode that propagates along the field. Depending on the parameters and geometry, the correction from the Song & Vasyliūnas (2011) model may or may not be appreciable. Nevertheless, this mode may be less likely to operate as a driver than an instability, which may be likely less important in driving the waves from the photosphere into the chromosphere.

Vranjes et al. (2008) questioned the importance of the Alfvén mode in the chromosphere when the ion–neutral collision frequency is greater than the ion gyrofrequency, a situation referred to as "unmagnetized" plasma. In a partially ionized plasma, the Alfvén wave is not limited to the frequency above the ion–neutral frequency or to high ionization. When the ionization is weak, an inertia-loading process becomes important below the ion–neutral collision frequency until the neutral–ion collision frequency (Song & Vasyliūnas 2005). Below the neutral–ion collision frequency, the whole fluid, plasma+neutral, acts like a single fluid and the Alfvén waves propagate at the Alfvén speed evaluated with the total mass density. This limit can be easily verified by summing the electron, ion, and neutral momentum equations in a three-fluid treatment, which leads to the single-fluid (plasma+neutral) description. As discussed by Song & Vasyliūnas (2011), the driver of the oscillations is the horizontal neutral flow oscillations in the photosphere, which cannot propagate upward if there is no viscosity. It is the magnetic field and neutral–plasma collisions coupling together that propagates the energy upward.

From the above discussion, in most areas of the chromosphere, the heating may be dominated by Alfvén wave heating. According to the Song & Vasyliūnas (2014) model, the heating rate in the chromosphere by damping the Alfvén waves from the photosphere is

$$Q(z) \approx Q_{\text{wave}} = \langle \delta V^2 \rangle_0 \sqrt{\rho_0 \rho}\, \frac{\omega_1^2}{\nu_{ni}} \left[(1-\alpha) + \frac{\nu_e \nu_{ni}}{\alpha\, \Omega_e \Omega_i} \right] \times \left(\frac{\omega_1}{\omega_c} \right)^{1-\gamma} \Gamma\left(\frac{3-\gamma}{2}, \frac{\omega_c^2}{\omega_1^2} \right), \quad (6)$$

$$\frac{1}{\omega_1^2} = \int_{z_0-\Delta}^{z} \frac{ds}{V_{At}\nu_{ni}} \left[(1-\alpha) + \frac{\nu_e \nu_{ni}}{\alpha \Omega_e \Omega_i} \right], \quad (7)$$

where V_{At} is the Alfvén speed (with total mass density, plasma + neutrals); ν_{ni}, ν_e are the neutral–ion and electron collision frequencies; Ω_e, Ω_i the electron and ion gyrofrequencies, respectively; $\nu_e = \nu_{en} + \nu_{ei}$; $\nu_{ni} = 7.4 \times 10^{-11} N_e T^{1/2}$; $\nu_{en} = 1.95 \times 10^{-10} N_n T^{1/2}$; $\nu_{ei} = 3.76 N_e T^{-3/2} \ln\lambda$; the temperature T is in Kelvin; and $\ln\lambda$ is the Coulomb logarithm. ω_c is the lower cutoff frequency of the spectrum of the source at the lower boundary, $\langle \delta V^2 \rangle$ is the square of the horizontal perturbation velocity, and γ is the power index of the wave energy spectrum at the lower boundary. The subscript 0 denotes values at the lower boundary of the chromosphere. Here the integration starts at $z_0 = 220$ km, and Δ is the step grid in the integration and is 10 km near the lower boundary given by the semi-empirical model. The second term in the brackets is due to Joule/Ohmic heating and the first term is frictional heating. The Poynting vector at the lower boundary is

$$S_0 \equiv \rho_0 V_{At0} \langle \delta V^2 \rangle_0. \quad (8)$$

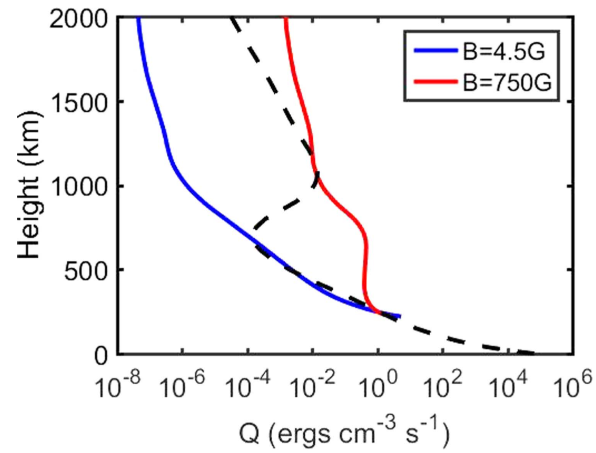

Figure 3. Wave heating rates, Q_{wave}, in erg cm^{-3} s^{-1} calculated based on Song & Vasyliūnas (2014) assuming the source of the waves is at 220 km and $\gamma = 5/3$. For $B_0 = 4.5$ G (blue line), the source is $S_0 = 10^7$ erg cm^{-2} s^{-1}. For $B_0 = 750$ G (red line), the wave amplitude is 60% as of $B_0 = 4.5$ G. The dashed black line is the reference of the radiative cooling.

The blue line in Figure 3 shows the heating rate for $B_0 = 4.5$ G with the source energy flux of $S_0 = 10^7$ erg cm^{-2} s^{-1} at the lower boundary $z_0 = 220$ km, $\omega_c = 2\pi/300$ s^{-1}, and $\gamma = 5/3$. Since the perturbation at the source is a power-law spectrum, the amplitude at that frequency is less than that of a single-frequency wave. For $S_0 = 10^7$ erg cm^{-2} s^{-1} and $B_0 = 4.5$ G, the peak amplitude is 9 km s^{-1}, which is close to the sonic speed.

For a given velocity perturbation amplitude, the Poynting flux in the strong field source is proportional to the field strength, as shown in Equation (8). However, when the field is stronger, the field lines are more rigid, which tends to resist large-amplitude perturbations. Therefore, we expect the velocity amplitude to be smaller than for the $B_0 = 4.5$ G case. We assume it to be 60% of the $B_0 = 4.5$ G case. Combining the factor 0.36 reduction in the wave amplitude squared with the factor of 167 increase in the field strength, the Poynting flux for $B_0 = 750$ G is assumed to be $S_{750\,\text{G}} = 60 S_0$. The peak amplitude of the perturbation is 5.4 km s^{-1}. The heating rate for $B_0 = 750$ G is shown as the red line in Figure 3. The black dashed line is the required radiative cooling rate—the blue curve in Figure 2, for reference.

It is clear that from 220 to 700 km, radiative cooling can be supported by the heating produced in the range of the ~4.5 G magnetic field, the blue line. Above 700 km, practically all wave energy in the weak field areas is dissipated. In other words, the wave energy in the weak field areas cannot support radiation above 700 km. The heating rate in the lower region for weak field is due to the Joule/Ohmic heating.

Since the Poynting flux in the network area, $B_0 = 750$ G, is much higher, or $S_{750\,\text{G}} = 60 S_0$, even though the damping rate of the waves is much lower, about 6%, through the lower region as discussed by Song & Vasyliūnas (2011), the net heating rate is still a few times higher in the network, resulting in a higher temperature in the network area in the lower region, consistent with observations (E. H. Avrett 2016, private communication). The remaining 94% of the wave flux propagate into the mid-altitudes and upper region as the field expands. The field expansion spreads the heat into a large horizontal area and the heat per area decreases. Given an expansion factor of 50, to be further discussed in Section 2.3.3,

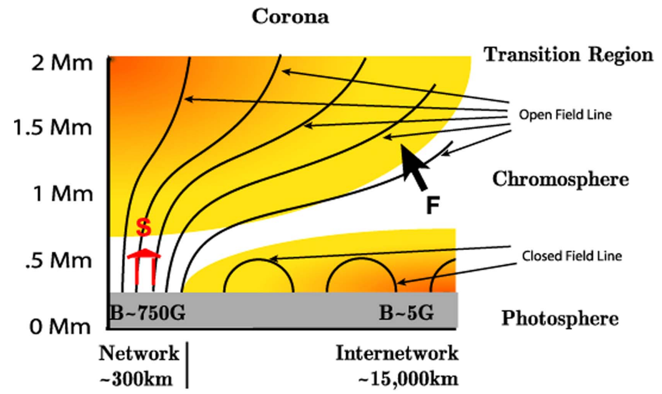

Figure 4. Illustration of the field line geometry (solid curves), not to scale. The strong magnetic field, which originated from the network area below the photosphere, expands in the upper chromosphere and is open into the corona. The weak magnetic field is randomly produced in the internetwork area and is mostly closed within the chromosphere. Orange areas indicate more efficient heating. The red open arrowhead indicates the Poynting vector that survived the damping in the lower region of network area, and the solid black arrow indicates the magnetic curvature force.

the $B_0 = 750$ G line in the upper region of Figure 3 is reduced approximately by the same factor. When the red line is reduced by an expansion factor of 50, it matches the dashed line at 2000 km in Figure 3. Frictional heating dominates in the strong field area.

2.3.3. Magnetic Field Geometry

The magnetic field distribution at the photospheric boundary is highly nonuniform with extremely strong fields in network areas of a few hundred kilometers wide. In the internetwork areas, on the other hand, the field is weak, as shown in Figure 4. As demonstrated in Section 2.3.2, at the lower boundary, the strong field of $\sim$750 G (or $\sim$1 kG at $z = 0$) and weak field of $\sim$5 G, around up from 4.5 G for a more general discussion, with an area coverage ratio of $\sim D/L = 1/50$, generally would satisfy the overall requirements (the total heating in the chromosphere and the total magnetic flux available for the corona). Due to the gravity, the thermal pressure decreases with height exponentially. The high magnetic pressure in the strong field area will become dominant as the height increases and the field will start expanding from the network area, a process that has been recognized by Gabriel (1976) and confirmed observationally (Giovanelli & Jones 1982). Since the strong field at the lower boundary is anchored below the photosphere and the internal circulation to be discussed in Section 2.4 is against the expansion, the expansion takes place significantly only above the lower region. The field in the mid-altitudes expands. When reaching the upper region, although the field is still strong, its gradient is small after force balance is reached with the neighboring supergranules. Therefore, the field lines in the mid-altitudes are bent to form a wine-glass-shaped geometry. The magnetic curvature force associated with the field line bending, as indicated by the thick solid black arrow in Figure 4, tends to balance the magnetic pressure force, and an equilibrium can, in principle, be attained. As will be shown in Section 2.4, the internal circulation will further reinforce the geometry, i.e., lengthening the stem of the wine glass and/or raising the height of the canopy.

Because the timescale of the large-scale equilibrium, of the order of the lifetime of a supergranule, $\sim$1 day, is much longer than the wave oscillation period of $\sim$5 minutes, the heating process can be treated as decoupled from the large-scale force balance processes. The heating affects the large-scale force balance only indirectly by modifying the temperature of the medium. The field lines can bend and/or expand in order to reach the equilibrium while the waves propagate and are damped along the field. Expression (6) includes the flux tube expansion effect due to magnetic flux conservation during the expansion. Expression (7) includes the field-bending effect, which cancels out the effect of integrating along the field from integrating along the height. However, the application of Expressions (6) and (7) can only be made semi-quantitatively. In a quantitative model, the magnetic field, density, and temperature have to be solved self-consistently with the heating rate and radiation cooling rate as well as Maxwell's equations. Among the critical parameters is the density of the medium, which determines the Alfvén speed and collision frequencies and is determined by the large-scale force balance.

Figure 3 has shown that practically all wave energy in the weak field areas is dissipated in the lower region, as indicated by the lower orange area in Figure 4, whether a field line is open, i.e., with one end connecting to the local photosphere and the other end to the corona in a field line merging model (e.g., Cranmer et al. 2007), or closed, i.e., with both ends connecting to the same supergranule and not reaching the transition region (e.g., Wedemeyer-Böhm et al. 2009). In our model we, preferring the latter situation, assume that the weak field areas are dominated by closed field lines. Waves propagate up from the photosphere and continuously feed from both ends of a weak field line. All wave energy is dissipated in the lower region. This heating process provides most of the energy required to support the radiation from the chromosphere because the weak field covers most of the lower region.

The field lines in strong field areas are mostly open in the domain of the chromosphere, although they may become closed through coronal loops to different supergranules. Because the magnetic field strength can be adjusted by the compression or expansion of a flux tube and is constrained by Maxwell's equations, the horizontal pressure balance between the weak field and strong field can be reached in principle with a possible localized vertical flow, the effects of which will be further treated in Section 2.4.

According to our model, most of the wave energy responsible for the heating of the upper region comes from the photosphere along the strong field, as indicated by the red, open, upward arrowhead in Figure 4, and then spreads out with the expansion of the strong field, as indicated by the upper orange area. Since the spatial expansion factor is $L/D \sim 50$ and the total open field flux from the photosphere is $\Phi \sim 750$ G $\times$ 300 km, the average field in the upper region is about $B \sim 15$ G with a small gradient toward the center of the network. If our 2D slab is about 30 Mm long in the third dimension, the dimension in-and-out-of the page in Figure 4, which shows half of the slab, the total magnetic flux contained in a supergranule is of the order of $\sim 1.5 \times 10^{20}$ Mx. The intersections of the network often form stronger fields and possibly more dynamic activities in particular when the intersecting networks have opposite field polarities, such as those reported by Attie et al. (2016). However, these interesting processes are not the focus of this study.

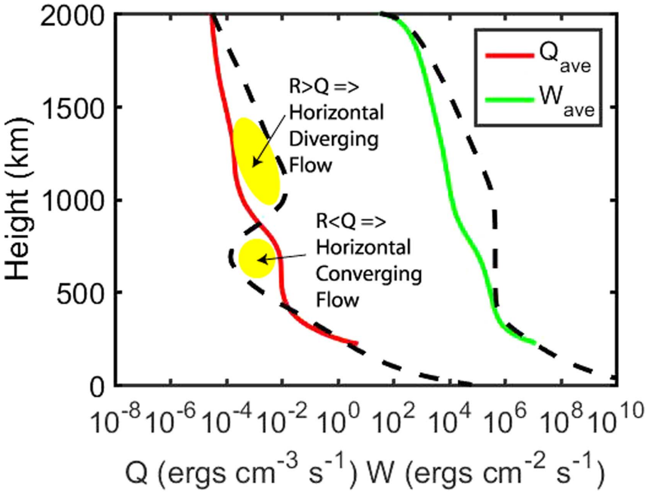

Figure 5. Average wave heating rate, $Q_{\rm ave}$, in erg cm^{-3} s^{-1} (red line) and height-integrated heating flux $W_{\rm ave}$ in erg cm^{-2} s^{-1} (green line). Dashed lines show the emission rate R and height-integrated emission flux W in Figure 2. Yellow regions indicate where horizontal flow is formed. For $R > Q$ ($R < Q$), the flow diverges from (converges toward) the network.

2.3.4. Horizontal Average of the Heating Rate

As discussed in Sections 2.3.2 and 2.3.3, the total heating in half of the model slab is provided by $\sim Q_{4.5\,\rm G}$ ~15,000 km from the internetwork and $\sim Q_{750\,\rm G}$ ~300 km from the network. The horizontally averaged heating rate,

$$Q_{\rm ave} = Q_{4.5\,\rm G} + Q_{750\,\rm G}/50, \tag{9}$$

and its height-integrated flux,

$$W_{\rm ave} = -\int_z^{2024} Q_{\rm ave}\, dz, \tag{10}$$

are shown in Figure 5. Figure 5 shows that the heating rates $Q_{\rm ave}$ and fluxes $W_{\rm ave}$ in our analytical model are similar to the radiative cooling rate R and integrated radiation flux W in the semi-empirical model, respectively, at the two boundaries of the chromosphere. The latter specifically indicates that our heating mechanism delivers the required heat to support the total radiation. These consistencies are derived from an evaluation of our analytic model using widely accepted representative parameters and geometry. These overall constraints indicate that the heating mechanism and model are inherently consistent with the essential processes governing the chromospheric processes.

The heating rate $Q_{\rm wave}$ and radiative cooling rate R, however, differ by about two orders near 700 and 1100 km in Figure 5, which correspond to about 26% in temperature difference, from Equation (4). Note that the field is nearly uniform near the top chromosphere and highly nonuniform in the lower region and undergoes transition in the mid-altitudes. The coverage-weighted average may represent a vertical cut of the chromosphere far from both the network and the center of the internetwork. The heating rate is in general expected to be higher closer to the network and lower closer to the center of the internetwork. In principle, this horizontal heating rate difference may be interpreted as a horizontal temperature difference, i.e., the temperature is generally slightly higher on the network side than on the center of the internetwork. The semi-empirical model (Avrett & Loeser 2008), on the other hand, may represent a horizontal average with a different weight function. Therefore, the difference between the two averages in Figure 5 may be due to different spatial weight functions and/or horizontal convection in the mid-altitudes, an issue that will need to be further discussed in Section 2.4.5.

In the above estimate, the total mechanical energy flux input is 2.2×10^7 erg cm^{-2} s^{-1}. The flux in the internetwork areas is totally dissipated and in the network, about 8%. The total dissipation, from the green line in Figure 5, is 1.1×10^7 erg cm^{-2} s^{-1}. This yields an average dissipation/heating efficiency of 50% for a whole supergranule. This efficiency would hold for a different total energy flux input, e.g., for half of the total input. The dissipated wave energy is on the same order of and sufficient to support the radiative loss. The remaining wave flux may be partially reflected at the transition region. However, the reflected waves will only be weakly damped and add a factor to the $Q_{750\,\rm G}$ term in Equation (9). This effect will not change the results in Figure 5 in the lower region but will add a fraction, which depends on the reflection coefficient, to the upper region. The penetrated wave flux propagates into the corona.

2.4. Formation of Circulation

We now analyze the convection effect that has been neglected in Section 2.3, an effect, recognized by Song & Vasyliūnas (2014), resulting from unevenly distributed heating.

2.4.1. Electric Current and Differential Motion of Species

In a single-fluid description, in principle, it is possible to find a static vertical radiative equilibrium condition for Equation (2) that also satisfies the static vertical force balance condition of Equation (1) for each of the strong field and weak field areas when allowing field expansion in the upper region, as discussed in Section 2.3.3. The horizontal static force balance between the strong field and weak field areas may be reached by expansion and compression of the strong field. However, because the magnetic field has to satisfy Maxwell's equations, a single-fluid description that satisfies all static conditions is impossible except for some singular cases, and circulation is in general inevitable. Solutions that are completely self-consistent with the collisional MHD equations and radiative loss, even qualitatively, deserve a series of separate studies. In this first study, which may be classified as semi-quantitative—meaning qualitative while all effects are constrained by observation and empirical knowledge to a reasonable range—we treat the ions and neutrals separately to examine the possible circulation, although we do not solve Maxwell's equations quantitatively, a practice often used in space physics (Song & Vasyliūnas 2013). The requirements of the steady-state Maxwell's equations are qualitatively implicitly included in our discussion. The momentum equations for the plasma and neutrals are

$$\rho_i (d/dt)\boldsymbol{V}_i = -\nabla P_i - \nu_{in}\rho_i(\boldsymbol{V}_i - \boldsymbol{V}_n) + \boldsymbol{J} \times \boldsymbol{B} + \rho_i \boldsymbol{g}, \tag{11}$$

$$\rho_n (d/dt)\boldsymbol{V}_n = -\nabla P_n + \nu_{ni}\rho_n(\boldsymbol{V}_i - \boldsymbol{V}_n) + \rho_n \boldsymbol{g}. \tag{12}$$

Because ions and neutrals experience different forces, there is a possible differential motion ($\boldsymbol{V}_i - \boldsymbol{V}_n$) that couples the two momentum equations, noting that from momentum conservation over collisions $\nu_{in}\rho_i = \nu_{ni}\rho_n$. The difference between the two equations is

$$\frac{d}{dt}(\boldsymbol{V}_i - \boldsymbol{V}_n) + \frac{kT}{m}\nabla \log\left(\frac{\alpha}{1-\alpha}\right) = \frac{\boldsymbol{J}\times\boldsymbol{B}}{\rho_i} - (\nu_{ni} + \nu_{in})(\boldsymbol{V}_i - \boldsymbol{V}_n). \quad (13)$$

Note that Equation (13) is a unique relationship only from the two-fluid treatment. A conventional single-fluid treatment would not be able to derive the circulation described below. The single-fluid momentum Equation (1) is obtained by the summation of Equations (11) and (12) and properly defining the bulk velocity and pressure, i.e.,

$$\rho(d/dt)\boldsymbol{V} + \nabla P = [\rho_i(d/dt)\boldsymbol{V}_i + \rho_n(d/dt)\boldsymbol{V}_n] + (\nabla P_i + \nabla P_n). \quad (14)$$

When the ionization fraction is low, the flow speed of the whole gas is similar to the neutral speed, and when the flow velocity is very small, the thermal pressure of the whole gas equals the summation of the thermal pressures of the two components.

In areas where the field is weak and electron collisions are heavy, such as in the lower region of the internetwork, the magnetic field does not play an important role in determining large-scale structures, although it guides the wave propagation and produces Ohmic heating. In the areas where the electron collision frequency is much less than the electron gyrofrequency, the electrons are frozen-in with the magnetic field, i.e., in the frame of reference of a quasi-steady-state supergranule, the electrons are not moving relative to the magnetic field. However, in 2D, the magnetic field may move horizontally along the network, for example, normal to the page of Figure 4. Since in 2D the current is also in this direction, it is possible to choose a frame of reference moving tangent to the network in which $\boldsymbol{V}_i = 0$. In this frame of reference, assuming to be the plane presented in Figure 4, electrons move horizontally and tangent to the network in the lower region, out of the page of Figure 4 if $\boldsymbol{B}$ is upward, producing a current that tends to expand the strong field area. Under chromospheric conditions, since the collision term is often much greater than the ionization gradient term in Equation (13), the current layer may be defined as the area where

$$\left|\alpha P \nabla \log\left(\frac{\alpha}{1-\alpha}\right)\right| \ll |\boldsymbol{J}\times\boldsymbol{B}|. \quad (15)$$

In areas dominated by collisions, the velocity difference in the current layer is

$$(\boldsymbol{V}_i - \boldsymbol{V}_n) = \frac{\boldsymbol{J}\times\boldsymbol{B}}{(\nu_{ni}+\nu_{in})\rho_i} \approx \frac{\boldsymbol{J}\times\boldsymbol{B}}{\nu_{ni}\rho} \sim \frac{V_{At}^2}{\nu_{ni} l}, \quad (16)$$

where l is the spatial scale of the current layer. From Equation (16), it is clear that the velocity difference is scaled with the Alfvén speed and the collision frequencies. In the areas where the collision frequencies are large and the Alfvén speed is small, the difference between the two species tends to be minimized and the two fluids move essentially together. In strong field areas and particularly in lower density areas, on the other hand, the relative speed between the plasma and neutrals can be significant although it may still be small numerically.

In the region without significant current or where the flow is mostly along the magnetic field, a differential flow may be maintained by the change in the ionization fraction, or

$$(\boldsymbol{V}_n - \boldsymbol{V}_i) \approx \frac{kT}{\nu_{in} m}\nabla \log\left(\frac{\alpha}{1-\alpha}\right). \quad (17)$$

Because the conditions in the chromosphere depend strongly on their location, we analyze the circulation in different regions separately in the next four subsections.

2.4.2. Circulation in the Lower Region

In general, in the lower region, both the ionization fraction, $\alpha \sim 10^{-3}$, and the collision time, $\sim 10^{-9}$ s, are extremely small, the density is high, and the magnetic pressure in the network is of the same order as the neutral thermal pressure in the internetwork. In a single-fluid treatment, a horizontal force balance may be achieved without significant large-scale flows. In a two-fluid treatment, the situation can be completely different because there is a possibility of relative motion between the two fluids. We now analyze this situation.

Outside of the network where the Alfvén speed is small, from Equation (16), the plasma and neutrals move together. The velocity difference may also be small inside the network in the magnetic field direction, along which $\boldsymbol{J}\times\boldsymbol{B} = 0$; see Equation (17).

The neutral thermal pressure is higher in the internetwork area and lower in the network area. This pressure gradient, from Equation (12), drives the (neutral) flow toward the network. The plasma is carried by the neutrals via collisions in the internetwork area. As the flow encounters the strong field, the plasma starts experiencing the electromagnetic force and slows down, while neutrals do not and continue moving. Collisions take place between the two fluids. As a result, the transition, the boundary between the network and internetwork, is broadened into a current layer of finite thickness, where a finite flow speed difference is maintained. If the magnetic field line is mostly vertically straight, from the horizontal component of the steady-state Equation (16), because α is small, the whole gas flow speed is

$$\boldsymbol{V} \approx \boldsymbol{V}_n \approx -\frac{\boldsymbol{J}\times\boldsymbol{B}}{\nu_{ni}\rho} \approx \frac{1}{2\mu_0 \nu_{ni}\rho}\nabla B^2. \quad (18)$$

This converging horizontal flow toward the network has been consistently observed (e.g., Attie et al. 2016). The thermal pressure also changes accordingly. Similarly but oppositely, because of the small ionization fraction in the lower region, the plasma pressure in the internetwork area alone is not sufficient to confine the strong magnetic field in the network area, and the plasma tends to flow into the weak field areas, as shown in Equation (11). Adding the two processes, the plasma velocity may change its sign from inward to outward while the neutrals continuously flow inward, a possibility that needs further studies when more detailed observational knowledge is available.

The outward plasma flow cannot be sustained in steady state unless there is a source of plasma in the strong field area. Additional ionization can be produced from the higher heating rate and hence higher temperature toward the center of the strong field as indicated by the $B_0 = 750$ G line in Figure 3. From Equation (17), an increase in the ionization fraction can sustain an inward neutral flow and outward plasma flow. In this process, a small fraction of the inward moving neutrals is ionized and flows outward due to the magnetic pressure gradient force. In this scenario, a strong magnetic field area without significant current can be maintained at the center of the network. The increase in the ionization is not sufficient to reduce appreciably the neutral density.

The horizontal neutral inflow is decelerated in the strong field area and, from the mass conservation, eventually diverges to vertical flow when it encounters the same flow from the opposite side of the network. A central question is whether it flows upward or downward. If the flow is diverged downward, the stagnation point is at the upper end of the lower region, and if upward, it is at the photospheric boundary.

To answer this question, we first examine the x-component, the horizontal direction in Figure 4, of the momentum Equation (1) in steady state. Combined with the 2D continuity equation, it can be written as

$$\frac{\partial}{\partial x}\left[\rho V_x^2 + P + \frac{B^2}{2\mu_0}\right] = -\frac{\partial \rho V_x V_z}{\partial z}. \tag{19}$$

Farther into the network area, the dynamic pressure decreases and the magnetic pressure increases. Along the stagnation streamline, equilibrium is reached with an effective pressure P_{eff} at the stagnation point (e.g., Russell et al. 2016),

$$\xi\rho_w V_{wx}^2 + P_w = P_{\text{eff}} + \frac{B_s^2}{2\mu_0}, \tag{20}$$

where $\xi < 1$ is a geometric factor and depends on the shape of the obstacle, and the subscripts s and w denote the strong and weak field areas, respectively.

We now examine the vertical component of the momentum equation. The hydrostatic equilibrium condition for the weak areas can be approximated as, from Equation (1),

$$P_w \approx P_{w0} e^{-\Delta z/H_{w0}}, \tag{21}$$

where $\Delta z = z - z_0$ is from the lower boundary to the height of interest. If no large-scale horizontal flow at the lower boundary of the chromosphere is assumed, we have

$$P_{w0} = P_{s0} + B_{s0}^2/2\mu_0. \tag{22}$$

When the gas from the weak field area flows into the strong field area along the stagnation streamline, the effective thermal pressure is

$$P_{\text{eff}} = P_w - B_s^2/2\mu_0 + \xi\rho_w V_{wx}^2. \tag{23}$$

Note that although the magnetic field has a tendency to expand and decrease in strength with height, the dynamic pressure of the inward flow tends to confine the expansion. We neglect the effect of the vertical magnetic field change. A vertical flow can be driven by the difference between this effective pressure and the static equilibrium pressure of the strong field area, P_s, from Equations (1) and (21)–(23),

$$\begin{aligned}\frac{dV_{sz}}{dt} &= -g\frac{H_0}{\Delta z}\log\left(\frac{P_{\text{eff}}}{P_s}\right)\\ &\approx -g\frac{H_0}{\Delta z}\log\left(1 + \frac{\xi\rho_{w0}V_{wx}^2}{P_{s0}}\right)\\ &\approx -g\frac{H_0}{\Delta z}\left(\frac{\xi\rho_{w0}V_{wx}^2}{P_{s0}}\right) < 0.\end{aligned} \tag{24}$$

Because the rhs of Equation (24) is negative, $dV_{sz}/dt < 0$, namely, the flow is downward and the stagnation point is at the height of the upper end of the lower region. In quasi-steady state, the flow speed at the lower boundary is

$$V_{sz0} \approx \left[2H_0 g\left(\frac{\xi\rho_{w0}V_{wx}^2}{P_{s0}}\right)\right]^{1/2} \sim \left(2H_0 g\xi\frac{P_w}{P_s}\right)^{1/2}\left(\frac{V_{wx}}{V_{\text{th}}}\right). \tag{25}$$

Given that for a supergranule the horizontal half-scale is 15,000 km and the lifetime is 1 day, $V_x \sim 0.17\ \text{km s}^{-1}$, the thermal speed $V_{\text{th}} \sim 10\ \text{km s}^{-1}$, $H_0 = 100$ km, $g = 0.27\ \text{km s}^{-2}$, $\xi = 0.8$, $P_w/P_s \sim 10^0$, and $V_{sz0} \sim 10^{-1}\ \text{km s}^{-1}$, consistent with the observed downdraft speed of $10^{(-1\sim-2)}\ \text{km s}^{-1}$ (Skumanich et al. 1975).

In summary, in the lower region, from Equation (18), there is a systematic flow from the middle of the internetwork toward the center of the network, an effect that might not be present in a single-fluid treatment. From Equation (24), this higher density gas from the internetwork sinks down along the strong magnetic field of the network, forming a downdraft, which was recognized by Gabriel (1976) and Parker (1978). Note that a major difference between Gabriel's circulation and that of Parker (1978) is that the horizontal flow, based on limb observation, is below the canopy in the former and is in the canopy height in the latter. We have shown that based on physical arguments the circulation should be just below the canopy. The continuity condition requires the formation of the convection cell as the cooler chromospheric gas flows down to below the photosphere in the network areas and is heated, and then reemerges from the internetwork areas. However, the upward flow is expected to be very weak because the horizontal scale of the internetwork is much larger than the vertical scale of the lower region. This cell is observed as half of a supergranule. The lower region of Figure 6 summarizes in 2D the circulation and geometry.

2.4.3. Horizontal Flow Below the Transition Region

As shown in Figure 3, the heating rate in the upper region above the network is more than the radiation rate and hence the average temperature is higher in this area. The higher temperature and hence higher pressure then drive a flow away from the network area. The expansive motion is in addition to the magnetic field expansion discussed in Section 2.3.4. In the upper region, the ion collision frequency is much smaller than the ion gyrofrequency and, in steady state, the ions can be approximated as frozen-in with the field, or $V_{i\perp} = 0$. The expansive neutral flow distorts the field geometry from its static equilibrium via collisions,

$$\delta[(\nabla \times \boldsymbol{B}) \times \boldsymbol{B}]_x = -\mu_0 \nu_{ni}\rho_n V_{nx}, \tag{26}$$

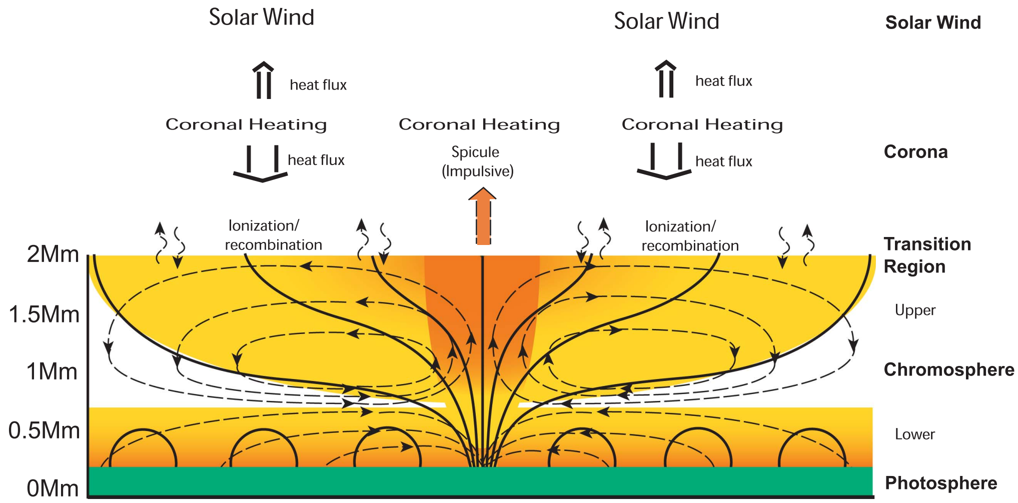

Figure 6. Model of the chromosphere with the size of a supergranule, not to scale, where the strong network magnetic field area is located in the center of the diagram rooted in the photosphere. The solid lines indicate the magnetic field lines and the dashed lines the convection streamlines of neutral flow. The orange-to-red colored regions indicate higher and increasing heating rates. The green region is the photosphere.

where δ denotes the deviation from the static equilibrium. The term in the brackets is the static field. In the conventional approach, it is a force-free field in the absence of an appreciable plasma pressure gradient. Because $\nu_{ni} \sim 10^3$ Hz, $B \sim 15$ G, the order of the circulation speed is

$$V_{nx} \sim \frac{V_A^2}{\nu_{ni} \Delta x} \sim \frac{10^4}{5 \times 10^2 \times 10^4} \sim 2 \times 10^{-3}\,\mathrm{km\,s^{-1}}, \quad (27)$$

significantly less than the supergranule circulation speed and in the opposite direction. Observationally, this corresponds to a less organized but underlying flow pattern from the network toward the middle of the internetwork. The circulation velocity is less than the fluctuation velocity but, averaged over a long period of time, say 1 day, the average flow may be able to reveal the circulation pattern. The large-scale horizontal flow maintains the upper surface of the upper chromosphere, the transition region, and brings heat horizontally to the entire upper chromosphere.

According to mass conservation, the large-scale horizontal neutral flow away from the network area is provided by the upward flow along the network. Our heating mechanism stops operating at the height where the ionization fraction is close to one. Because the density of the corona is very low, the large vertical temperature gradient at the transition region is highly stable to the buoyancy instability under quiet-Sun conditions. A large downward flow from the corona into the chromosphere is not expected during quiet times. The energy and mass transfer between the chromosphere and corona are mostly by the heat flux, ionization, and recombination, as well as sporadic launches of spicules (De Pontieu et al. 2011), which are formed when the heating along the center of the strong field is so strong that the kinetic energy carried by the upward moving gas is sufficient to pierce through the stabilizing transition region. The spicules bring a large amount of chromospheric neutral particles which, while continuing their upward motion, produce more emissions before they are fully ionized.

2.4.4. Downward Flow from the Top of the Internetwork

As the flow expands away from the network area, the heating rate and the temperature decrease gradually, and the density increases to maintain the horizontal pressure balance. In the middle of the internetwork, the colder and heavier neutral flow encounters a similar circulation flow from the neighboring network areas and both sink downward.

In steady state, the downdraft of the neutral flow in the middle of the internetwork is slowed down by the increasing magnetic pressure through collisions and distorts the field from static equilibrium. From Equation (16), the distortion and the downdraft flow satisfies

$$0 \approx -\delta[(\nabla \times \boldsymbol{B}) \times \boldsymbol{B}]_z + \mu_0 \nu_{ni} \rho V_{nz}. \quad (28)$$

Given that near the upper boundary of the lower region, $\sim$700 km, $N_n \sim 10^{14}\,\mathrm{cm^{-3}}$, $\nu_{ni} \sim 5 \times 10^2$ Hz, $B_x \sim 50$ G, the downward flow speed is 2×10^{-4} km s^{-1}, about a factor of 10 less than the horizontal speed. The lower temperature and hence a higher recombination rate further helps the downdraft and cross-field motion of the flow.

The lower boundary of the canopy separates the region of strong horizontal magnetic field from the high β gas below. The momentum of the downdraft discussed in the last subsection is eventually balanced by the thermal pressure at the top of the lower region, where neutrals and plasma move together and B is very small as discussed in Section 2.4.2. In the mid-altitudes, 700–1000 km, from Equation (1),

$$\frac{dV_z^2}{2dz} = -\frac{kT}{m}\frac{\partial \log P}{\partial z} + \frac{[(\nabla \times \boldsymbol{B}) \times \boldsymbol{B}]_z}{\mu_0} - g$$
$$\approx -\left(\frac{kT}{m}\frac{\Delta \log P}{\Delta z} + g\right) + \frac{[(\nabla \times \boldsymbol{B}) \times \boldsymbol{B}]_z}{\mu_0}. \quad (29)$$

The first term on the rhs is close to zero for near hydrostatic equilibrium. The field is dominated by the horizontal component, which decreases its magnitude with height. The magnetic force is upward. The lhs is then positive and the downward flow slows down. A stagnation area, similar to that discussed in Section 2.4.2, is formed at the top of the lower region. It is interesting to note that the temperature shown in Figure 1 increases more rapidly with height in the middle chromosphere than in the upper region, a potential piece of evidence for the magnetic effect in Equation (29).

2.4.5. Return and Upward Flow in the Mid-altitude

As the downdraft in the upper region stops, to conserve the mass, the flow is diverged to a horizontal flow toward the network area in the mid-altitudes. When the flow returns to the network area in the mid-altitudes, it arrives at the stagnation area as discussed in Section 2.4.2 but on its upper side.

The horizontal return flow has an additional effect. A question is whether it can be formed or not. In Section 2.3.4, we noted that although the horizontally averaged heating rate and the average radiative loss rate are similar at the bottom and the top of the chromosphere, they are significantly different in the middle range. A question is whether the difference is a deficiency of the model or physical. For a quasi-steady-state stratified chromosphere, far away from the areas of significant vertical flow, the steady-state dissipation Equation (2) is

$$\boldsymbol{V} \bullet \nabla[\log(P\rho^{-5/3})] = \frac{2}{3}\frac{Q-R}{P}. \tag{30}$$

When $Q \neq R$, a flow is produced as indicated by the yellow shaded areas in Figure 5, and a gradient in entropy is needed. Because the temperature and hence the entropy is higher on the network side, the gradient of the entropy on the left points toward the network and is negative in our coordinates. When $Q > R$, the horizontal convection, $V < 0$, is toward the network. When $Q < R$, the flow, $V > 0$, is away from the network. In Figure 5, $Q > R$ from 500 km to 900 km and $Q < R$ for $z > 900$ km. The resulting flow is toward the network below 900 km and away from the network above 900 km. This flow direction is in general consistent with the horizontal flow as demonstrated above and shown in Figure 6. We think the numerical difference between the flow reversal indicated in Figure 6, 1000 km, and the one in Figure 5, ~900 km, may be a result of the simple field model in our estimate and/or different weighting functions in the semi-empirical model as discussed in Section 2.3.4. Nevertheless, if the flow is significant enough, from Equation (30), there should be a difference between the Q derived in our model and the R calculated from the semi-empirical model. This convection effect may at least partially explain the difference between Q and R in Figure 5.

From Figure 1, the ionization fraction starts increasing above 700 km. Since in the network the field is mostly vertical, the magnetic force is weak in the vertical direction. The rhs of Equation (17) is positive as α increases, resulting in an upward flow. There are two effects that further help the flow go upward. First, there is overheating, when the heating rate is much greater than the radiative loss, in the network at this height as shown in Figure 3, and this overheating is maximum at around 700 km, corresponding to the stagnation point. The higher pressure built up by overheating tends to drive flow away from the stagnation. We have shown that the gas below the stagnation flows downward, and similarly, the gas above the stagnation flows upward. Second, as discussed in Section 2.4.3, mass conservation requires an upward flow to sustain the horizontal flow moving away from the network at the top chromosphere. Therefore, the flow moves upward in the network above the lower region.

Combining Sections 2.4.3–2.4.5 completes the upper circulation cell, as illustrated in Figure 6.

The flows in the upper and lower circulation cells are in principle separated by a separatrix at a height of about 700 km, which corresponds to the minimum of the electron density in Figure 1.

3. Summary and Discussion

We have analyzed the chromosphere in the range from 220 km above the Sun's surface to the transition region according to multifluid collisional MHD theory including radiation. We emphasize that our model is guided and hence is semi-quantitatively consistent with zeroth-order observations. All processes employed in the model are based on "classical" theory and no "anomalous" processes are invoked or needed. The model involves several concepts, such as radiative loss and magnetic flux tube expansion, which have been widely employed in modeling the chromosphere. The new ingredients are the dependence of the heating rate on the magnetic field resulting from the strong damping of a broadband Alfvén wave in partially ionized plasma, and the formation of circulation cells associated with nonuniform heating and differential motion between plasma and neutrals.

The most important result of the model is the interpretation and description of the processes as well as the possible observational features of the chromosphere, which are summarized in Figure 6. It illustrates the structure and processes of a supergranule during quiet conditions. The figure is not to scale, but with a horizontal width of ~30,000 km and vertical height of ~2000 km. The dimension in the direction normal to the page is of the order of a supergranule, i.e., ~30,000 km, as well. The strong field area in the middle of the figure is ~600 km around 220 km altitude with $B \sim 750$ G. The field from this area is "locally open." The chromosphere is divided into two regions by the minimum of the electron density at ~700 km altitude. The lower region dominated by "locally closed" weak field, ~5 G, is heated by Ohmic heating and almost all wave energy from the photosphere in this region is damped. The heating in this region provides almost all of the required chromospheric emission, the most challenging problem in the outstanding question of coronal heating. Although the horizontal scale of the network is small, because the Alfvén speed is large, the total amount of the wave flux from the photosphere in this area is comparable to that from the entire internetwork. The waves in the network areas, however, are only weakly damped and produce heat via frictional heating. Most of the wave flux continues propagating upward along the magnetic field and being weakly damped in the upper region by frictional heating.

As the thermal pressure decreases with height, the strong field in the network expands, driven by the magnetic pressure gradient force. The expansion of the network area spreads the strong field from the network area into the entire upper region and forms the magnetic canopy. Along with the field expansion, the waves from the network area also spread to the whole upper region. The continuous weak damping of these waves provides radiation in the upper region. About 90% of the wave energy flux from the network area is able to survive the chromospheric damping and reach the transition region. It is possible that part of the wave flux is reflected at the transition region. The reflected wave flux will most likely propagate along the field back to the network area with only weak damping. The flux that penetrates through the transition region propagates into the corona and provides the energy source for further coronal heating and launching of the solar wind. Additional heating processes, in which the plasma neutral collision effects may not be important, are required to take place around the temperature maximum in the corona.

Overall, based on the semi-empirical values, the total amount of the energy flux from the network area is about the same order as that from the vast internetwork area. However, almost all wave energy from the internetwork is damped but only about 10% of the energy from the network is. Averaged over a supergranule, the efficiency of the damping/heating of this model is about 50%.

Due to the nonuniform magnetic field from the photosphere, which results in nonuniform heating, and the overall gravitational stratification, which maintains large-scale horizontal force balance, two convection cells are formed on each side of the network. In order to describe such a circulatory motion surrounding a relatively stable field structure, the differential motion between plasma and neutrals has to be described. In our model, the plasma is mostly frozen-in with the field, except in the internetwork areas of the lower region. If the magnetic field is in quasi-steady state, there is no appreciable plasma flow perpendicular to the field in the 2D plane. The circulations shown in Figure 6 are neutral motions. The differential motion is very small in the weak field areas of the lower region and can be large when the collision frequencies are small in the upper region. The differential motion between the neutrals and plasma, where streamlines intersect the field lines nearly orthogonally in Figure 6, corresponds to localized currents that further distort the field.

The primary driver of the lower cell is the neutral thermal pressure gradient force from the internetwork toward the network, an effect that might not be present in a conventional single-fluid treatment. The quasi-steady-state flow is maintained by ion–neutral collisions. The primary driver of the upper cell is the thermal expansion of the higher heating rate in the strong field area. The convection cells distort field geometry from static equilibrium, which has been derived, e.g., through force-free conditions in conventional treatments. The distortion is such that it further reinforces the wine-glass-shaped magnetic field, in particular elongating the stem of the wine glass.

There are similarities between Figure 6 of the present work and Figure 6 of Wedemeyer-Böhm et al. (2009), which was constructed based on Judge (2006) and Rutten (2006, 2007) as well as observations and numerical simulations. Both figures indicate that supergranules driven below the photosphere are the building blocks of the chromospheric structures. Both have closed field lines in the internetwork areas and wine-glass-shaped open field lines above the network. The main differences are that the horizontal supergranular flow converges toward the network in the lower chromosphere in our model and in the photosphere in Wedemeyer-Böhm et al. This converging flow may produce a longer stem of the wine glass. We have an additional circulation cell in the upper region based on physical requirements. The diverging horizontal flow near the top of the chromosphere helps the expansion of the magnetic field, and the return flow in the mid-altitudes further lengthens the stem of the wine-glass shape of the field geometry. The heating mechanism in our model is specific and without artificial elements. In our model, shock heating does not need to play an important role even if shocks are observed and might play a secondary role. The heights specified in the two figures are different, which may result from our use of the semi-empirical model.

Even though our model is primitive in this early stage without a realistic magnetic field model, sophisticated radiation models, and a quantitative constraint on the horizontal force balance, with a reasonable wave power input from the photosphere, it successfully semi-quantitatively reproduces the heating/radiation profile in the lower region (blue line in Figure 3), the overall heating–radiation bulge (green line in Figure 5), and the average heating rate (red line in Figure 5), when convection effect is included. Again, all these are achieved within the observed thickness of the chromosphere without invoking "anomalous" processes, and all parameters are evaluated according to classical theoretical expressions and the semi-empirical model. A model of the field expansion is critical for any further comparison.

What has been achieved in this study for the first time is that the structure and controlling processes for the chromosphere under quiet conditions are understandable in a semi-quantitative manner with horizontal and vertical force balances, magnetic flux conservation, energy conservation, reasonable wave power from the photosphere, and sufficient heating rate to support the radiation in each region and area. The semi-quantitative estimates are supported by the ballpark observed properties of the chromosphere. This model provides a zeroth-order control of the quiet chromosphere. Most importantly, this is achieved with classical processes. In retrospect, the objective of the Song & Vasyliūnas (2011) model was to show that collisional damping is able to provide sufficient damping of the Alfvén waves. The lower boundary of the chromosphere was set to $z = 0$ km. However, the damping appears too strong that there is little wave energy left to heat the upper chromosphere. With the process presented in this study, when all constraints are considered, the radiation below 220 km appears too large and cannot be supported by the 10^7 erg cm^{-2} s^{-1} wave energy flux. This realization can serve as a warning to all chromospheric modeling studies: because the chromosphere is a very complicated system, it cannot be studied as individual isolated elements. Furthermore, we would ask all observers to revisit their observations and interpretations. For example, if convection cells do exist, the interpretation of Doppler shifts may highly depend on the height where the measurements are made. Because our theoretical modeling analyses are based on the radiative, collisional, partially ionized, multifluid MHD theory, if a numerical MHD simulation that is based on classical theory deviates substantially from these identified controlling processes, their results may need careful examination and verification. In particular, if excessive dissipation is invoked in the simulation, justification has to be provided without non-physical reasons, such as to stabilize the code. There is evidence that shows a simulation code for a similar collisional multifluid MHD system (Tu & Song 2016) can provide robust solutions without invoking numerical/artificial dissipation effects.

The author thanks V. M. Vasyliūnas for many valuable discussions and specific comments and suggestions, E. H. Avrett and S. R. Cranmer for useful discussions, and Y. Huang for preparing the figures. This study was supported by NSF grant AGS-1502549 and NASA grant NNX12AD22G to the University of Massachusetts Lowell.

ORCID iDs

P. Song https://orcid.org/0000-0001-5938-8108

References

Anderson, L. S., & Athay, R. G. 1989, ApJ, 346, 1010
Aschwanden, M. 2005, Physics of the Solar Corona: An Introduction with Problems and Solutions (New York: Springer)
Attie, R., Innes, D. E., Solanki, S. K., & Glassmeier, K.-H. 2016, A&A, 596, A15
Avrett, E. H., & Loeser, R. 2008, ApJS, 175, 229
Bello Gonzalez, N. B., Franz, M., Pillet, V. M., et al. 2010, ApJL, 723, L134
Carlsson, M., & Leenaarts, J. 2012, A&A, 539, A39
Cox, D. P., & Tucker, W. H. 1969, ApJ, 157, 1157
Cranmer, S. R., van Ballegooijen, A. A., & Edgar, R. J. 2007, ApJS, 171, 520
De Pontieu, B., Martens, P. C. H., & Hudson, H. S. 2001, ApJ, 558, 859
De Pontieu, B., McIntosh, S. W., Carlsson, M., et al. 2007, Sci, 318, 1574
De Pontieu, B., McIntosh, S. W., Carlsson, M., et al. 2011, Sci, 331, 55
Dungey, J. W. 1961, PhRvL, 6, 47
Edlén, B. 1943, ZA, 22, 30
Erdelyi, & Fedun 2007, Sci, 318, 1572
Fossum, A., & Carlsson, M. 2005, Natur, 435, 919
Gabriel, A. H. 1976, RSPTA, 281, 399
Giovanelli, R. G., & Jones, H. P. 1982, SoPh, 79, 267
Goodman, M. L. 2000, ApJ, 533, 501
Jess, D. B., Mathioudakis, M., Erdelyi, R., et al. 2009, Sci, 323, 1582
Judge, P. 2006, in ASP Conf. Ser. 354, Solar MHD Theory and Observations: A High Spatial Resolution Perspective, ed. J. Leibacher, R. F. Stein, & H. Uitenbroek (San Francisco, CA: ASP), 259
Kalkofen, W. 2007, ApJ, 671, 2154
Khodachenko, M. L., Arber, T. D., Rucker, H. O., & Hanslmeier, A. 2004, A&A, 422, 1073
Khomenko, E., & Collados, M. 2012, ApJ, 747, 87
Leake, J. E., Arber, T. D., & Khodachenko, M. L. 2005, A&A, 442, 1091
Martínez-Sykora, J., De Pontieu, B., & Hansteen, V. 2012, ApJ, 753, 161
Mihalas, B. W., & Toomre, J. 1982, ApJ, 263, 386
Narain, U., & Ulmschneider, P. 1990, SSRv, 54, 377
Narain, U., & Ulmschneider, P. 1996, SSRv, 75, 453
Osterbrock, D. E. 1961, ApJ, 134, 347
Parker, E. N. 1978, ApJ, 221, 268
Rammacher, W., & Ulmschneider, P. 2003, ApJ, 589, 988
Reardon, K. P., Lepreti, F., Carbone, V., & Vecchio, A. 2008, ApJL, 683, L207
Russell, C. T., Luhmann, J. G., & Strangeway, R. J. 2016, Space Physics: An Introduction (Cambridge: Cambridge Univ. Press)
Rutten, R. J. 2006, in ASP Conf. Ser. 354, Solar MHD Theory and Observations: A High Spatial Resolution Perspective, ed. J. Leibacher, R. F. Stein, & H. Uitenbroek (San Francisco, CA: ASP), 276
Rutten, R. J. 2007, in ASP Conf. Ser. 368, The Physics of Chromospheric Plasmas, ed. P. Heinzel, I. Dorotovic, & R. J. Rutten (San Francisco, CA: ASP), 27
Schmutzler, T., & Tscharnuter, W. M. 1991, A&A, 273, 318
Schure, K. M., Kosenko, D., Kaastra, J. S., Keppens, R., & Vink, J. 2009, A&A, 508, 751
Shelyag, S., Cally, P. S., Reid, A., & Mathioudakis, M. 2013, ApJ, 776L, 4S
Skumanich, A., Smythe, C., & Frazier, E. N. 1975, ApJ, 200, 747
Soler, R., Carbonell, M., & Ballester, J. L. 2013, ApJ, 767, 171S
Song, P., & Vasyliūnas, V. M. 2010, Chines J. Space Sci., 30, 289
Song, P., & Vasyliūnas, V. M. 2011, JGR, 116, A09104
Song, P., & Vasyliūnas, V. M. 2013, in Modeling the Ionosphere-Thermosphere System, ed. J. D. Huba, R. W. Schunk, & G. V. Khazanov (Washington, DC: AGU), 201
Song, P., & Vasyliūnas, V. M. 2014, ApJL, 796, L23
Song, P., Vasyliūnas, V. M., & Ma, L. 2005, JGR, 110, A09309
Spitzer, L., Jr. 1956, Physics of Fully Ionized Gases (New York: Interscience)
Tu, J.-N., & Song, P. 2013, ApJ, 777, 53
Tu, J.-N., & Song, P. 2016, JGR, 121, 11861
Ulmschneider, P. 1981, A&A, 12, 297
Ulmschneider, P. 2001, in Encyclopedia of Astronomy and Astrophysics, ed. P. Murdin (Bristol: IOP Publishing), 2260
Ulmschneider, P., Rammacher, W., Musielak, Z. E., & Kalkofen, W. 2005, ApJL, 61, L155
Ulrich, R. K. 1996, ApJ, 465, 436
Vasyliūnas, V. M., & Song, P. 2005, JGR, 110, A02301
Vecchio, A., Cauzzi, G., & Reardon, K. P. 2009, A&A, 494, 269
Vernazza, J. E., Avrett, E. H., & Loeser, R. 1981, ApJS, 45, 635
Vranjes, J., Poedts, S., Pandey, B. P., & De Pontieu, B. 2008, A&A, 478, 553
Wedemeyer-Böhm, S., Lagg, A., & Nordlund, Å. 2009, SSRv, 144, 317
Wiegelmann, T., Thalmann, J. K., & Solanki, S. K. 2014, A&ARv, 22, 78
Withbroe, G. L., & Noyes, R. W. 1977, ARA&A, 15, 363
Wöger, F., Wedemeyer-Böhm, S., Uitenbroek, H., & Rimmele, T. R. 2009, ApJ, 706, 148
Young, P. R., Del Zanna, G., Landi, E., et al. 2003, ApJS, 144, 135
Zaquarashvili, T. V., Khodachenko, M. L., & Soler, R. 2013, A&A, 549A, 113Z